








Bayesian inference elucidates fault-system anatomy and resurgent earthquakes induced by continuing saltwater disposal

Hannes Vasyura-Bathke ¹, Jan Dettmer ²✉, Katherine Biegel ², Rebecca O. Salvage², David Eaton ², Nicolas Ackerley ³, Sergey Samsonov ⁴ & Torsten Dahm ¹

An earthquake sequence in western Canada exhibits resurgent aftershocks, possibly in response to persistent, post-mainshock saltwater disposal. Here, we reduce uncertainty in mainshock source parameters with joint inference of interferometric synthetic aperture radar and seismic waveform data, showing that the mainshock nucleated at about 5-km depth, propagating up-dip toward the injection source, and arresting at about 2-km depth. With precise hypocenter relocations and Bayesian inference, we reveal that four subparallel faults were reactivated, likely part of a regional, basement-rooted graben system. The reactivated faults appear to be truncated by a conjugate fault that is misoriented for slip in the present-day stress regime. The nearest saltwater disposal well targets a permeable Devonian reef in direct contact with Precambrian basement, atop a ridge-like uplift. Our observations show that a fault system can be activated more than a decade after saltwater disposal initiation, and continued disposal may lead to a resurgence of seismicity.

¹Helmholtz Centre Potsdam, German Research Centre for Geosciences GFZ, Potsdam, Germany. ²University of Calgary, Calgary, Canada. ³Canadian Hazards Information Service, Natural Resources Canada, Ottawa, ON, Canada. ⁴Canada Centre for Mapping and Earth Observation, Natural Resources Canada, Ottawa, ON, Canada. ✉email: jan.dettmer@ucalgary.ca

An earthquake sequence commenced in November 2022 at a previously relatively seismically quiescent location near the town of Peace River in north-central Alberta, Canada (Fig. 1). The moment magnitude (M_W) 5.2 mainshock on November 30 was preceded by four $M_W > 4.0$ foreshocks and was followed by a prolonged aftershock sequence, including two moderate earthquakes on March 16, 2023 (M_W 4.5 and 4.6) (Fig. 2). There is a considerable industrial activity in the vicinity of this sequence, including heavy oil recovery using steam injection as well as massive saltwater disposal (SWD) into formations at various depths¹.

The origin of this sequence, herein called the Peace River earthquake sequence, has been debated. The Alberta Energy Regulator (AER) initially assessed the earthquakes to be of natural tectonic origin², citing a lack of proximal hydraulic fracturing activity, the absence of changes in deep fluid disposal rates during the preceding year, and an initial estimate for focal depth (6 km) that it seemed to be deeper than expected for induced earthquake triggering at this location. However, the mainshock and initial aftershocks, together with other seismicity clusters in the general area, have since been investigated and interpreted to be induced¹, primarily by SWD into a deep disposal well located about 3.5 km east of the mainshock epicenter (well I in Fig. 2). The present study aims to help elucidate the origin of this sequence, through analysis of the source mechanisms and spatiotemporal evolution of seismicity after the fault system was activated.

Injection-induced earthquakes generally occur on pre-existing faults and have source characteristics that are similar to natural events³, although they typically nucleate at shallower depths⁴ and may exhibit spatiotemporal activation patterns consistent with an

expanding pore-pressure triggering front⁵. Documented cases of induced seismicity within ~500 km distance of the Peace River earthquake sequence include events triggered by enhanced oil recovery⁶, gas production⁷, saltwater disposal^{8–10} and hydraulic fracturing^{11–14}. Although infrequent, natural tectonic events have been recorded in this region, notably the 2001 M_W 5.4 Dawson Creek earthquake⁴, located ~200 km west of the Peace River earthquake sequence. The 2001 earthquake occurred in a structural setting that is similar to the 2022 sequence, characterized by basement-rooted extensional faults of Carboniferous age^{15,16}. These crustal-scale normal faults are comprised of a series of secondary NW-trending normal faults (e.g., Tangent Fault, Fig. 1) that are intersected, and possibly truncated, by conjugate graben structures (e.g., Whitelaw graben, Fig. 1). The graben structures are filled with syn-tectonic sediments (Stoddart Group) and the normal fault systems are step-like, characterized by a set of parallel faults that delineate structural corridors^{15,17}. Collectively known as the Dawson Creek Graben Complex (DCGC), this regional fault system marks the collapse of the early Paleozoic Peace River Arch (PRA), a paleo-emergent landmass that was fringed by a massive carbonate reef complex (Leduc Formation). The fringing reef is >300 m thick and is characterized by exceptionally high permeability (up to 10^{-12} m²), making it well-suited for SWD.

This study rigorously characterizes and interprets the Peace River earthquake sequence using several approaches. The prolonged sequence of >130 aftershocks between November 23, 2022, and March 23, 2023 (Fig. 3) is investigated by precise relocation analysis¹⁸. Using Bayesian joint inference¹⁹, mainshock rupture characteristics are inferred by combining interferometric

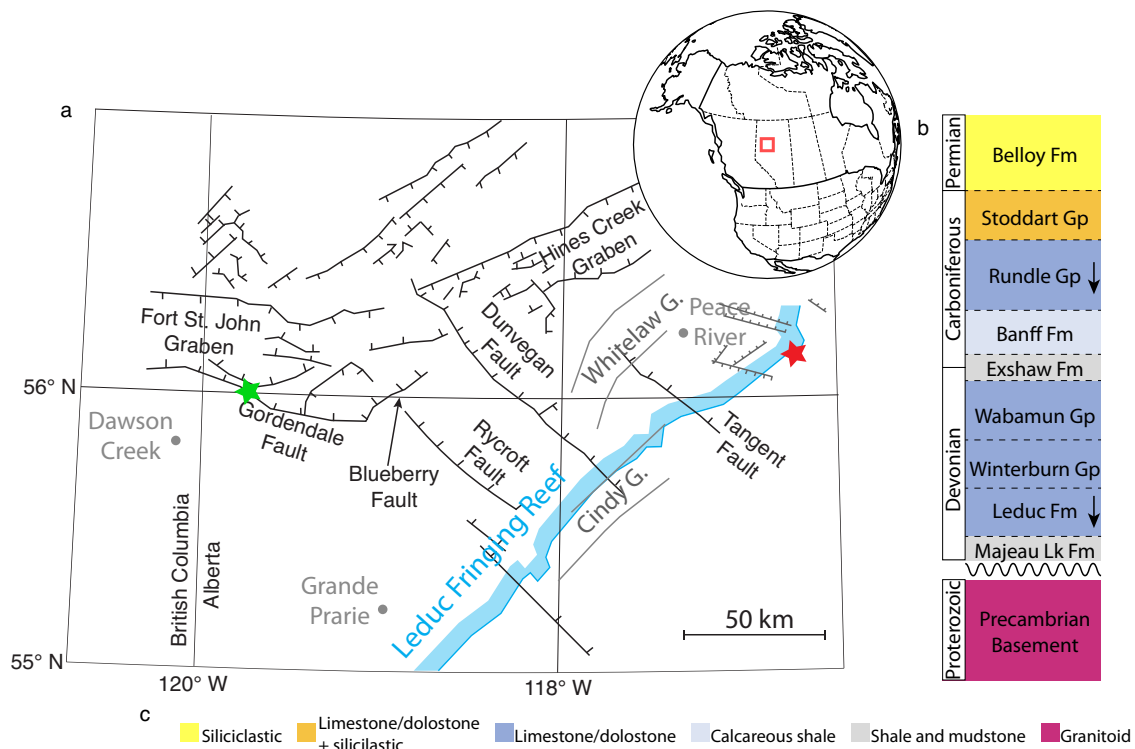


Fig. 1 Geologic setting of the Peace River earthquake sequence. **a** Geologic setting of the Peace River earthquake sequence in western Canada (red box) and location of the M_W 5.2 mainshock (red star). The sequence occurred near the eastern end of the Peace River Arch (PRA), an early Paleozoic emergent landmass surrounded by epicontinental seas and fringed by a Late Devonian reef system (Leduc Formation). The PRA collapsed in the Late Carboniferous, forming extensive grabens bounded by basement-rooted normal faults^{16,99}. Several grabens are intersected by conjugate faults. The M_W 5.4 Dawson Creek earthquake in 2001 (green star) was a natural event with a reverse source mechanism that reactivated a normal fault in the Precambrian basement⁴. **b** Simplified Paleozoic stratigraphy of the study region (arrows highlight SWD formations), with **c** generalized lithology¹⁰⁰.

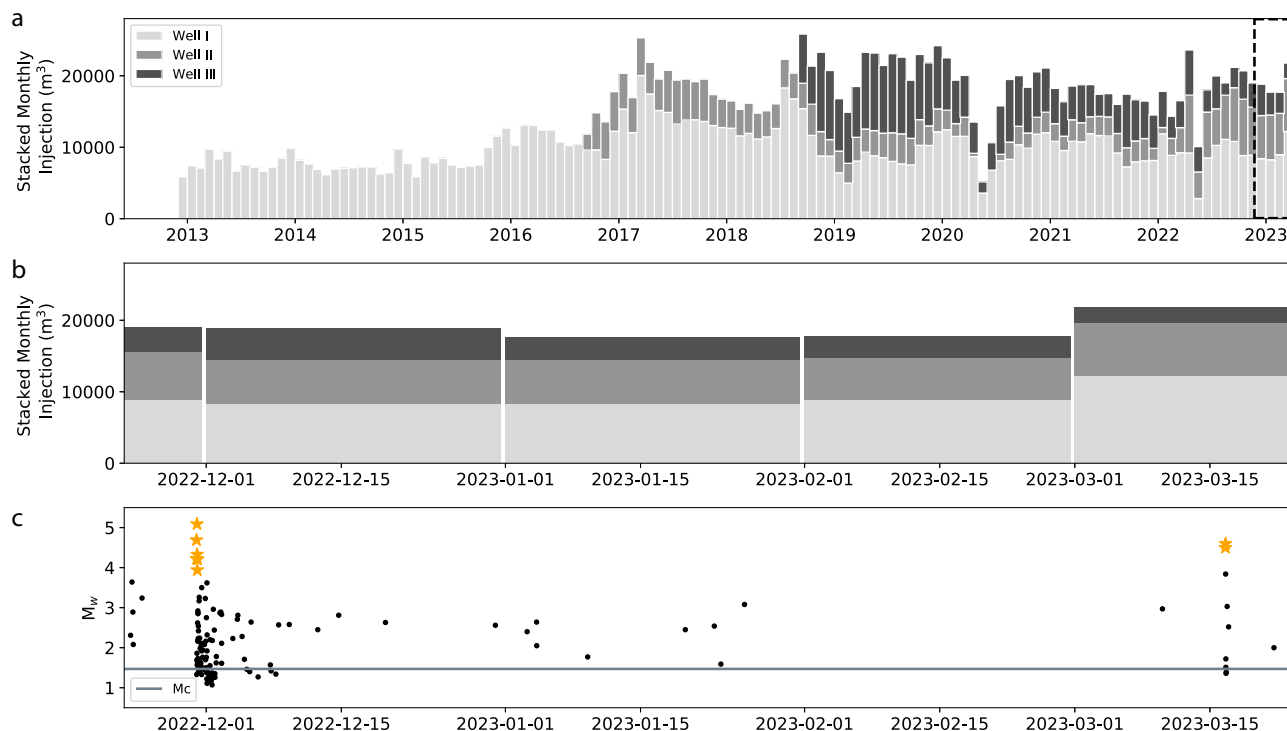


Fig. 2 Saltwater injection and seismicity. **a** Stacked monthly injected volume of saltwater at three disposal wells located near the epicenters of the Peace River earthquake sequence. Well I has operated since December 2012 and is injecting into the Leduc Formation, while wells II and III are injecting into shallower formations. The dashed box indicates the extent of timespan for **(b)** and **(c)**. **b** Stacked injected volume of saltwater at three wells near the epicenters from November 2022 to March 2023, where M_w is estimated from M_l for the smaller events using the relation in Supplementary Fig. S7. Public data sources are limited to total monthly injected volumes. **c** Time series of moment magnitudes (M_w) for the Peace River earthquake sequence, between November 23, 2022, and March 23, 2023. The estimated magnitude of completeness is 1.47 and is shown as a gray horizontal line. Events analyzed in this work are shown in orange. Saltwater injection continued after the mainshock, with a reported increase in March 2023.

synthetic aperture radar (InSAR) with seismic data. Source mechanisms of seven fore- and aftershocks are studied using Bayesian inference with seismic data alone. The earthquake distribution reveals a fault-system anatomy with four nearly parallel NW-trending faults that are favorably oriented for slip in the present-day stress regime, truncated by a conjugate fault that is misoriented for slip. Seismic and geodetic rupture imaging of the M_w 5.2 mainshock provides the absolute location with low uncertainty and resolves deep nucleation, with arrest at the top of the Precambrian basement and peak slip of 0.24 m. Some areas of the imaged fault system appear to have not yet ruptured, pointing to possible future seismic risks.

Results and discussion

We present earthquake hypocenter relocations for 132 events²⁰ and detailed rupture characteristics for eight of the largest events. For comparison with previous analysis of this sequence¹, the events considered here are confined to the epicentral region of the previously defined central cluster, but extend the time window to include later aftershocks (see Supplementary Section 7 for the magnitude of completeness). The mainshock is studied by joint inference of InSAR and seismic data obtained with the Bayesian Earthquake Analysis Tool (BEAT¹⁹). The BEAT software enables the analysis of a variety of source models with rigorous uncertainty quantification, including centroid moment tensors, kinematic rectangular faults, and finite faults. Particular care is taken to model the temporal and spatial dependence of data noise and rigorously assess data fits. Accounting for this dependence is important when combining data types in joint inference to ensure that the information contributed by the various types is weighted

appropriately without subjective input²¹ (see “Methods” for details).

Reactivation of four subparallel faults. The relocation was carried out using a double-difference method¹⁸ to refine relative hypocenter locations. The relocations are constrained by catalog arrival picks and cross-correlation data computed for event pairs recorded at the same station. Up-sampling in the frequency domain was applied to increase the temporal resolution of cross-correlation estimates. The improvement in location accuracy is demonstrated by a reduction of residual errors and removal of depth artifacts (see Supplementary Fig. S9 and “Methods” for details). Furthermore, bootstrap and jackknife uncertainty quantification demonstrates that uncertainties in terms of 95% confidence intervals for relative locations are 93 m in the EW direction, 63 m in the NS direction, and 128 m in depth. In map view (Fig. 4b), aftershocks reveal an apparent NE-trending cluster of seismicity; however, a fault with this strike direction is inconsistent with inferred nodal planes (Fig. 3). When visualized in three dimensions, it is evident that the seismicity occurs along a series of NE-dipping features. By careful visual inspection, the event distribution was separated into four clusters. The clustering was then evaluated by applying least-squares regression to fit planes to each cluster (Fig. 4d). The planar fit of events is improved when considering four planes, justifying the choice of four clusters. The four fault planes interpreted from the regression are labeled F1, F2, F3, and F4 (Fig. 4). These have strike values of 290°, 289°, 295°, and 297° (ordered from F1 to F4), and dip angles of 52°, 55°, 54°, and 50°. Therefore, this analysis in 3D reveals a basement fault system consisting of four subparallel faults, with individual faults being separated by between 500 and

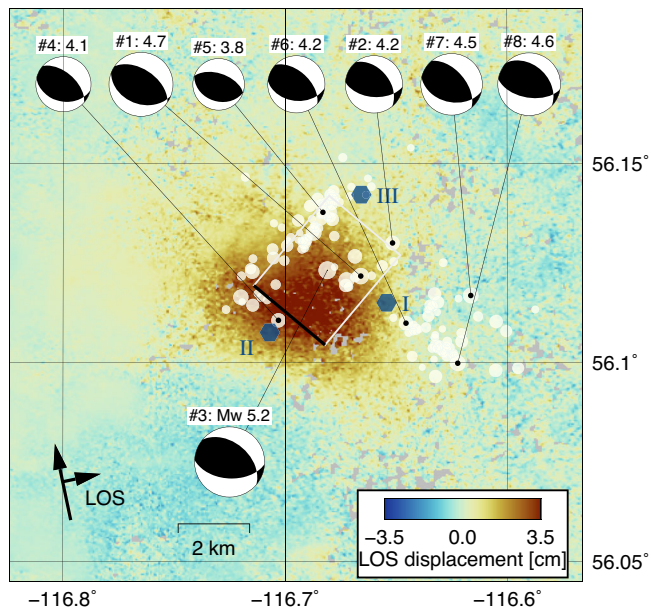


Fig. 3 Relocated seismicity, injection wells and surface deformation.

Relocated seismicity (white circles) between November 23, 2022, and March 23, 2023, plotted on a ground displacement image from InSAR (background color). Circle sizes are scaled by magnitude, and blue hexagons show saltwater injection wells within the map area. The focal mechanisms are our solutions for eight events of $M_W \geq 3.8$ and are numbered chronologically (Supplementary Tables S2 and S3). The rectangle is the surface projection of a northeast dipping rectangular rupture area inferred from seismic and InSAR data, where the thick line represents the top of the fault. Displacements in the satellite line of sight (LOS) were calculated from InSAR data between November 13, 2022, and December 12, 2022.

600 m. The seismicity is mainly confined to the area covered by the Leduc fringing reef and where a basement ridge exists (Fig. 4).

Mainshock nucleates deep and arrests near top of the Precambrian basement. Using functionality available in BEAT, we applied a systematic analysis to investigate the mainshock source characteristics that were not previously considered. The mainshock is first modeled with a deviatoric moment tensor (Fig. 5a and Supplementary Fig. S1), which resolves a reverse fault that is consistent with a previously published solution¹ but constrained by InSAR and seismic data and includes rigorous uncertainty quantification. Our uncertainty estimates suggest that the rupture can be reasonably explained by slip on a planar fault (i.e., a double-couple, DC, mechanism). The modest compensated linear vector dipole (CLVD) component of between 16 and 22% obtained by this analysis could be due to the spatial extent of the ruptured asperity which is not fully explained by the point-source assumption. The predicted InSAR scenes provide a general match to the observed line-of-sight (LOS) deformation of ~ 3.5 cm (toward satellite) (Supplementary Fig. S2). A region of ~ -0.8 cm deformation (away from satellite) is also predicted. Variance reductions (VR) for the CMT source are (>81 , >72 , and $>54\%$) indicating that the point-source approximation of CMTs cannot match all InSAR features; hence, fault models that consider spatial extent are justified.

Next, the results for a kinematic rectangular source model are considered. We apply uniform prior probabilities for strike and dip between 0 and 360° and 0 and 90°, respectively. Such models can produce results for conjugate faulting planes²². However, applying a uniform prior on mean slip between 0 and 0.5 m based

on empirical earthquake scaling laws²³, resulted in a unique fault that dips to the northeast (Figs. 5b and 6). Notable for an $M \sim 5$ event is the resolution of kinematic model parameters with low uncertainties, which is enabled by joint inference using three InSAR displacement maps and seismic data. Note that the displacement maps contain deformation signals from aftershocks. However, the large magnitude and shallow depths of the mainshock cause the dominant deformation (see “Methods” for more details). Fault location is resolved with uncertainties of <200 m in the lateral direction and <100 m in the vertical direction. The rectangular source model resolves strike at 310°, dip at 45° and rake at 118°, with angular uncertainties of $<2^\circ$. The fault is estimated to be 2.7 km long (along strike) with 0.5 km uncertainty (95% credibility-interval width, see “Methods” for details) and 4.75 km wide (along dip) with 0.3 km uncertainty (Fig. 7). The average slip on this fault area is ~ 0.2 m with an uncertainty of 0.06 m. The duration of moment release is 6.7 s with 0.3 s uncertainty and the rupture propagates across the fault in 1.3 s, resulting in a rupture velocity of 3 km/s which is similar to the shear-wave velocity at the rupture depths. The rupture nucleated at the bottom of the fault, displaced 0.5 km from the fault center (Fig. 5b) at ~ 5 -km depth, and propagated upward with a reverse sense of motion to ~ 1.9 -km depth, where basement rocks are in direct contact with the disposal zone (Leduc Formation). While the kinematic solution constrains the evolution of rupture with time, it does not resolve the spatial distribution of slip.

Figure 7a shows observed and predicted InSAR data for the mainshock obtained with a kinematic rectangular fault rupture model^{24,25}. For the three scenes, VRs are >82 , >78 , and $>86\%$, a clear improvement over fits achieved with the CMT point source model. This is consistent with the notion that the more complex model explains more data features. The seismic waveforms include extensive coda (Fig. 7b and Supplementary Fig. S3), likely due to the layering structure of the WCSB. The predictions generally fit these features (Supplementary Fig. S3). For the mainshock with rectangular-fault parametrization, VR mean values of $>58\%$ for Z components and $>35\%$ for T components (Supplementary Fig. S4) are achieved. Note that some stations (e.g., RV.PECRA, Fig. 7) show near-field effects in the form of long-period signals. The modeling of seismic waves with QSEIS included near-field effects²⁶ which match the observed near-field effects to a limited extent. Seismic amplitude spectra are generally fit more closely than waveforms (Fig. 7 and Supplementary Fig. S4), due to the lesser information content, specifically the lack of information about phase in the spectrum. In summary, the data fits indicate that inferred parameter values reflect the observations, which raises confidence in our results.

Finally, we consider Bayesian finite fault inversion^{19,27,28} to study the spatial distribution of slip based on only InSAR data. An extended fault which employs strike and dip from the rectangular solution (fixed at the maximum posterior probability values) with square patches of 1 km². Patch size was determined by sensitivity analysis²⁹ to avoid excessive regularization. Furthermore, the smoothest model regularization is treated as hyper parameter which avoids subjective choice and applies smoothing consistent with the data information¹⁹. The extended size is 7 km along strike and 6 km in dip direction, with a total of 42 patches. The top of the fault is located at 1-km depth. The results (Fig. 5c) provide constraints on the peak slip which is not possible with the rectangular fault. The maximum slip of 25 cm occurs at 2.5-km depth and has uncertainty from 20 to 29 cm (Fig. 5c presents uncertainty by ellipses on the rake vectors). The rupture is approximately ellipsoidal with the long axis along the rake direction (115°), long radius of 3 km, short radius of 2 km, and most slip occurring between 2- and 4.5-km depth. Taken

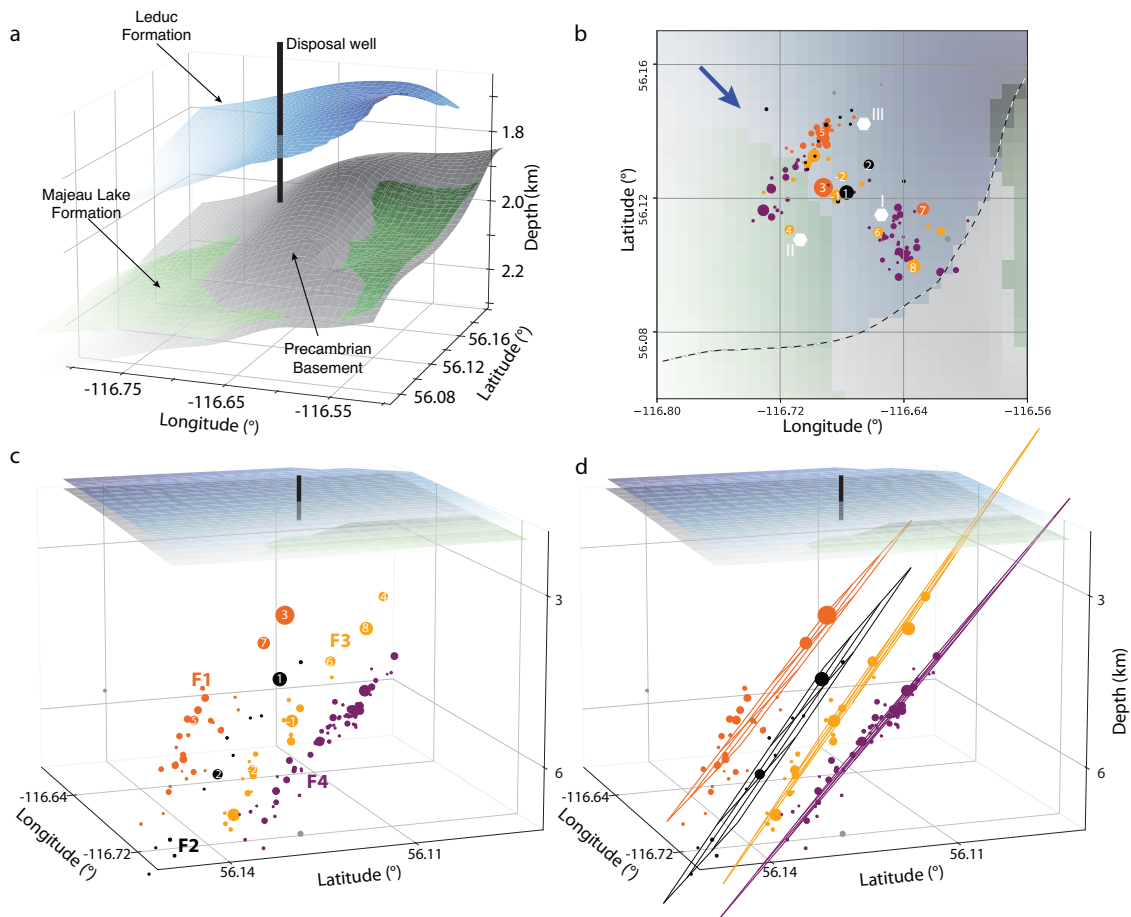


Fig. 4 Earthquake relocations, clustering and fault-system anatomy. **a** Surfaces showing selected formation tops, with disposal well I (black), top of Leduc Formation (blue), top of Majeau Lake Formation (green), and top of Precambrian basement (gray)⁹³. The Leduc fringing reef is in thickness and has a near-vertical margin. A basement ridge is evident from the missing Majeau Lake section. **b-d** Interpretation of earthquake locations (circles, radius proportional to magnitude) in terms of four clusters (F1: orange, F2: black, F3: yellow, F4: purple) that delineate four dipping faults. The extent of the Leduc Formation (blue), Majeau Lake Formation (green), and Precambrian basement (transparent gray) are shown⁹³. In **(b)**, well locations for three wells (white hexagon) and reef edge (dashed line) are shown. The view direction in **(c)** and **(d)** is along the arrow shown in **(b)**. Specific events considered in the discussion are numbered chronologically, starting with two foreshocks (negative numbers) that are not considered with Bayesian inference (see Supplementary Table S3). **d** Visualization of best-fit planes for the four clusters.

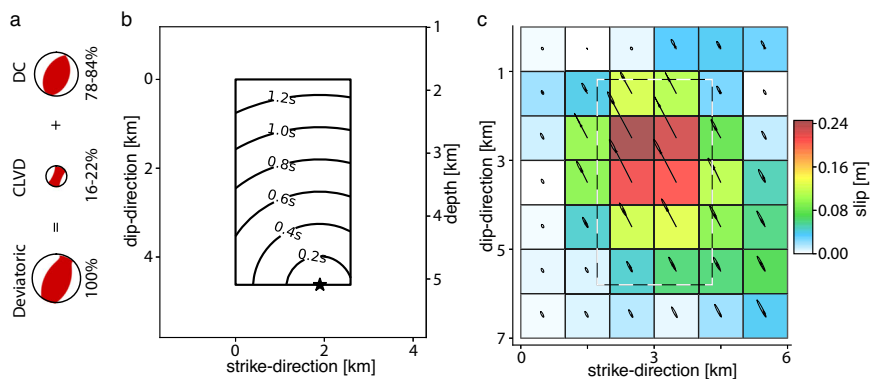


Fig. 5 Mainshock inference results for different parameterizations. **a** Deviatoric moment-tensor solution and its decomposition into CLVD and DC for the mainshock. **b** Planar view on the rectangular fault with rupture fronts (solid black, increments in 0.1 s after nucleation time), nucleation point (black star), and the rupture extent (thick black rectangle). **c** Slip distribution for the mainshock inference from static finite-fault model. The rake direction for each patch (black arrows), 95% confidence intervals (black ellipses), and the size of the rupture inferred from the rectangular source (dashed) are shown.

together, the rectangular- and finite-fault results suggest relatively little slip along the tip line zone of the rupture, with slip increasing to a maximum value near the top of the fault. The static finite-fault solution overall resulted in the highest VRs for

the three InSAR displacement maps (>90, >89, and >82%). Compared to previous work¹ we resolve a slip distribution that is not highly smooth but shows peak slip in the upper part of the asperity. In addition, peak slip is lower (0.2–0.29m) in our results

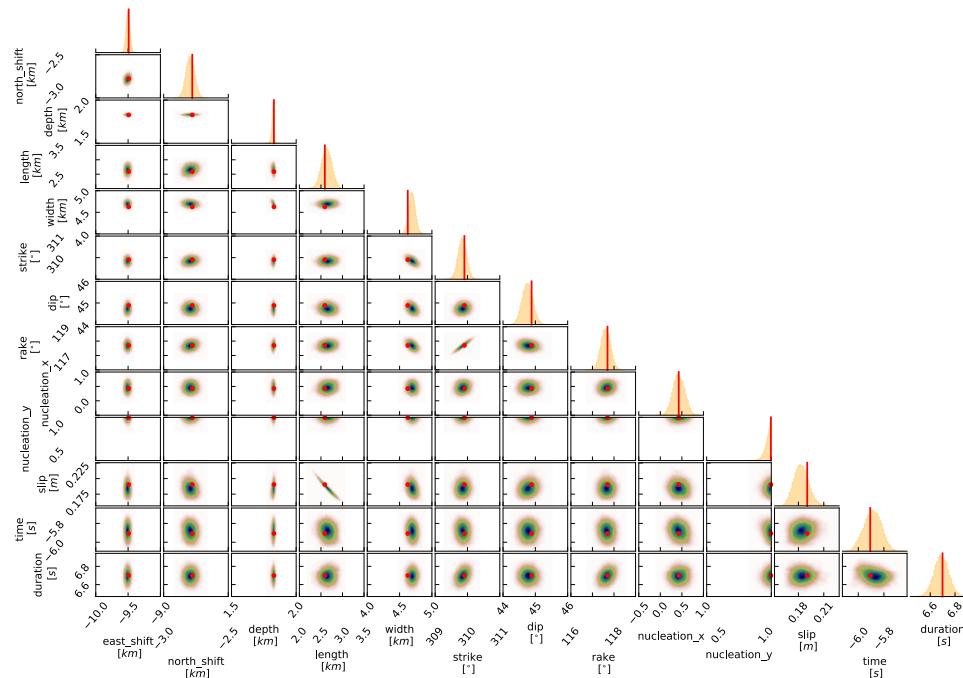


Fig. 6 Inferred mainshock kinematic rectangular fault parameters. Inversion results for the mainshock with kinematic rectangular source constrained by InSAR and seismic data in terms of marginal and joint-marginal posterior probability densities. Note the small uncertainties and reduction in parameter correlations compared to inversion with only seismic data (Supplementary Fig. S5).

and the rupture is elongated in the direction of rake (approximately 120°). Since the location and orientation of the receiver fault plane are well-constrained by our joint inference (Fig. 6), and since we estimate correlated residual errors through the non-Toeplitz covariance matrices, we consider features in the slip distribution as robust³⁰.

Fore- and aftershocks on multiple subparallel faults. Figure 8 summarizes CMT results obtained from Bayesian inversion of seismic data for seven earthquakes of $M_W > 3.8$ with two 3D views. The agreement between observed and predicted data for these events is comparable to those achieved for the mainshock. Focal mechanisms for all events (Supplementary Table S2) are similar oblique-reverse with rake angles varying between 100° and 120° (where 90° is pure reverse). The inferred faults strike between 300° and 320° and dip at angles between 37° and 55° . Such steep dip is atypical for reverse faults, but consistent with the reactivation of normal faults within the DCGC.

The 3D view in Fig. 8b illustrates that the moment-tensor solutions activate a complex fault architecture in several stages, with ruptures that are highly consistent between faults and with the highest magnitude at shallow depth. A similar architecture consisting of parallel en echelon faults has been observed in the case of a different earthquake sequence triggered by SWD, also located near the southern flank of the Peace River Arch¹⁰. Most aftershocks are located on the deepest fault below the M5.2 earthquakes. Notably, the M_W 4.5 aftershock on March 16, 2023 (No. 7) appears to rupture the same asperity as the mainshock, after a 4-month delay.

Combining InSAR and seismic data reduces uncertainty. The mainshock was well recorded by three InSAR displacement maps and seismic data, which is remarkable considering the relatively small magnitude of M_W 5.2. Bayesian inference can be employed to combine these data sets in joint inference without the requirement of choosing subjective data weights (see “Methods”).

As a result, the rupture location and characteristics exhibit low uncertainty (Fig. 6). In comparison, uncertainties for results obtained exclusively from seismic data (Supplementary Fig. S5) are much larger. In addition, the results from seismic data show strong parameter correlations and multiple modes in the marginal probabilities. These effects vanish for the joint inference (Fig. 5), which furnishes evidence that complementary information is contained in the various data sets. For example, uncertainties for fault location (including depth), fault extent, and rupture nucleation are reduced substantially. Kinematic parameters (e.g., nucleation point and rupture duration) are improved as a result of the constraints provided by the static InSAR data (e.g., fault orientation and slip amount). Since the absolute location of the mainshock has the lowest uncertainty, we applied a spatial shift to the relative hypocentre locations derived from the double-difference algorithm to achieve consistent absolute locations.

Fault-system anatomy. At first glance, the map pattern of epicentral locations (Fig. 3) suggests activation of conjugate NE- and SE-trending faults. However, clustering in 3D leads to our interpretation of four steeply dipping, subparallel faults. The seismicity on these faults concentrates along a NE-trending linear feature that we interpret as a conjugate fault that was not activated. Hence, seismicity appears to concentrate along the intersection of well-oriented faults with a misoriented fault, possibly due to stress concentrations at fault terminations³¹. This geometry is consistent with the structural style of Carboniferous faulting in the PRA region (e.g., Tangent fault and Whitelaw graben) as well as step-wise parallel sets of normal faults³². Both the rectangular-fault and finite-fault models show that the rupture arrests at the same location where aftershocks are observed to cluster, providing further evidence of an intersecting fault at this location.

The pattern of seismicity is also consistent with fault orientations relative to the present-day stress since the conjugate

fault that truncates the NW-trending faults is misoriented for slip. Stress inversion³³ results (Supplementary Fig. S14) from the eight events with $M_W \geq 3.8$ show that maximal compressive stress (σ_1) is nearly horizontal ($25.3^\circ \pm 4.4^\circ$). The orientations of σ_2 and σ_3 exhibit low uncertainty in their orientations, but with uncertain plunges. The ratio of σ_2 to σ_3 (stress shape ratio, R) is 0.89. Therefore, the four activated faults are favorably oriented to the current stress field³³, and the conjugate fault is not activated because of unfavorable orientation in the current stress field. According to our model, seismicity concentrates near fault intersections and activates slip on a system of four favorably oriented, subparallel faults. While carrying out stress inversion with eight similar focal mechanisms provides only limited constraints, the inferred directions are plausible and broadly consistent with regional stress.

Natural or induced? Discerning whether the Peace River earthquake sequence was natural or induced is an important question, with potential ramifications that extend beyond SWD to include regulatory frameworks for other types of industrial activities¹ including carbon capture, utilization and storage (CCUS) and development of enhanced geothermal systems. Various approaches have been developed to discern if an earthquake (sequence) was induced, including quantitative probabilistic frameworks^{34,35} and questionnaire-based schemes^{36–38}. The applicability of questionnaire-based schemes for rapid assessment of induced events, including this sequence, is currently under investigation³⁹.

It has been argued that the Peace River earthquake sequence was induced¹, primarily due to SWD into the Leduc fringing reef. If this interpretation is correct, it makes the mainshock in this sequence the largest human-induced earthquake in western Canada, to date, and implies an exceptional time lag of more than a decade between the onset of injection and fault activation. Proximity to the crystalline basement is a key geological risk factor for induced seismicity⁴⁰ and it is notable that, unlike elsewhere in the WCSB, the Leduc Formation at this location directly overlies the Precambrian basement (Fig. 4). This direct contact increases the likelihood that a hydrological connection exists between the disposal formation and deep-seated faults, thus favoring an induced origin. As a further test, we have considered whether a temporal correlation exists between injection and seismicity. Unfortunately, injection data are only available as monthly averages. Nonetheless, we applied a cross-correlation and reshuffling test⁴¹ to search for a causal correlation between the injection rate into the Leduc disposal well and the seismicity rate, including aftershocks. This test indicates a significant (>95% confidence) correlation between these time series, with the highest correlation peak at a 51-month lag time, and secondary peaks above 95% confidence at 42- and 70-month lag times (Supplementary Fig. S7). Although a more precise correlation is not possible due to the 1-month granularity for the publicly available injection data, this result supports the conclusion that SWD likely played a key role in triggering this sequence¹.

Implications for injection-induced seismicity risk. The sequence activated the four faults with resurgent characteristics, possibly exacerbated by continued saltwater disposal after the mainshock. The sequence initiated on F3 with foreshocks at 4.4- and 5.3-km depth on November 23 and 24, respectively. The next two foreshocks on November 29 occurred on F2 at 3.7 and 5.6-km depth. The mainshock (No. 3 in Fig. 4) occurs on F1, rupturing from 5-km to 1.9-km depth. It is followed by two aftershocks on F3 at 3.7- (November 30) and 5.8-km (December 1) depth. We also observe that most aftershocks occur down-dip of the main rupture on F1 and on faults F2-F4. However, the M_W

4.5, March 16, 2023 aftershock occurred on F1, at the SE edge of the asperity ruptured by the mainshock with nearly 4 months delay (No. 7 in Fig. 4). The resurgence was preceded by a 2-month period of quiescence and coincides with an increase in disposed volume (Fig. 2). During this resurgence, substantial seismicity was only observed in this SE area with ruptures occurring on F1, F2, and F3.

The deepest fault (F4 in Fig. 4) hosts more aftershocks than F1-3, but no foreshocks. There are three events of $M_L > 4$, all on November 30. Note that only M_L estimates are available for these events which show a consistent bias of 0.86 higher than M_W estimates for the catalog (Supplementary Fig. S8). The center region of F4, located beneath the disposal well, does not contain notable seismicity. Ruptures due to natural earthquakes on similar faults to the west were shown to extend to much greater depths⁴ than observed here. It is therefore possible that the faults inferred by our study may extend much deeper than the asperities activated to date.

The inferred upward migration of foreshock hypocenters, as well as the up-dip propagation of the mainshock rupture in our geometric fault model, favors a cascade nucleation model⁴² that progresses from deeper to shallower levels. This ‘retrograde’ earthquake nucleation pattern is opposite to the rupture direction based on models of outward propagating triggering fronts⁴³. The up-dip rupture direction may reflect trade-offs that result from the superposition of the effects of downward diffusion of pore pressure with depth-dependence of instability on a rate-state friction-controlled fault⁴⁴. As noted previously¹, the exceptional latency period of 11 years between the start of injection and onset of seismicity likely reflects the prolonged time required to sufficiently pressurize faults that intersect the enormous regional saline aquifer system hosted within the Leduc fringing reef.

Methods

Data. Three interferograms (InSAR) derived from synthetic aperture radar data acquired by the Sentinel-1 and Radarsat Constellation Mission (RCM) satellites were processed by using the GAMMA software⁴⁵ (Supplementary Table S1). The topographic phase was corrected using the advanced spaceborne thermal emission and reflection radiometer digital elevation model (ASTER)⁴⁶ and interferograms were filtered with a Goldstein adaptive phase filter⁴⁷. Finally, interferograms were unwrapped with a minimum cost-flow algorithm^{48,49} to obtain the final displacement map employed in the inference (Fig. 7).

Seismic waveforms were rotated to radial (R), transverse (T) and vertical (Z) components and T and Z components were used in the analysis (Fig. 7 and Supplementary Fig. S3). For the smallest event, 6 Z and 7 T were retained after quality control and for the largest event 17 Z and 23 T components. The waveforms were corrected for instrument response, filtered between 40- and 10-s periods, and cropped to 130 s after the predicted P-wave arrival. This processing focuses predominantly on P and S waves. Seismic amplitude spectra are based on waveforms filtered between 40 and 7 s periods and provide additional information for the same 130-s time window. Note that amplitude spectra do not consider phase information and can be considered for stations where waveform fits are poor.

Modeling of data. Data predictions for InSAR data are based on Green’s Functions (GFs) computed with the PSGRN/PSCMP software⁵⁰ which computes the co- and post-seismic deformation, geoid and gravity changes for a viscoelastic, layered halfspace (Supplementary Table S4). Data predictions of seismic waveforms and amplitude spectra are based on GFs computed with QSEIS²⁶ and include near-field effects. To resolve source location, a 1-km

spacing for GFs is computed in the source region with a 2-Hz sampling rate⁵¹. All predictions assume a one-dimensional layered elastic halfspace^{52,53} (Supplementary Table S4).

Bayesian inference. To study the earthquake sequence, the Bayesian Earthquake Analysis Tool (BEAT) is applied¹⁹ which utilizes nonlinear Bayesian inference with sequential Monte Carlo sampling⁵⁴. The BEAT software is versatile and can be applied with various source models (full centroid moment tensors with unknown source-time function, kinematic rectangular faults, static and kinematic finite faults) and utilizes a variety of geodetic and seismic data.

In Bayesian inference, the unknown model parameters are considered to be random variables and probabilities express degrees of belief^{55,56}. Therefore, uncertainty quantification is intrinsically addressed. Bayes' theorem expresses the posterior probability density for a vector of N observed data \mathbf{d} and M model parameters \mathbf{m} as

$$p(\mathbf{m}|\mathbf{d}) = \frac{l(\mathbf{m})p(\mathbf{m})}{p(\mathbf{d})}, \quad (1)$$

where $l(\mathbf{m})$ is the likelihood function, $p(\mathbf{m})$ is the prior information, and $p(\mathbf{d})$ is a normalizing constant that does not need to be considered for this work. BEAT estimates the posterior $p(\mathbf{m}|\mathbf{d})$ with a sequential Monte Carlo (SMC) sampler⁵⁴.

Joint inference and noise covariance estimation. Data errors, including theory errors stemming from the choice of the Earth velocity model and source parametrization, play a crucial role in parameter and uncertainty estimates in Bayesian inference^{57,58}. Some assumptions about the noise statistics are required to employ the method while others are commonly made to further simplify the application. For example, the type of statistical distribution must be assumed while the parameters for the assumed distribution may be assumed or estimated. We employ data covariance estimation that has been shown to address both errors due to the measurement process and due to theory assumptions (e.g., velocity model), it does not rely on assumptions about uncertainties that may exist in the assumed velocity model and does not have notable computational cost²¹, as explained below.

This work considers joint inference with three data types: Seismic waveforms, seismic amplitude spectra⁵⁹, and displacement maps derived from synthetic aperture radar data. We assume that the noise observed on each data type is independent of the noise observed on the other types. Gaussian-distributed noise is assumed with zero mean and the noise covariance matrices are estimated from the data. Each data type comprises observations collected from different locations in space and time. For simplicity, the following considers these observations are combined into one data vector for each type. However, we will later explain specific details about the data. The mathematical treatment is sufficiently general to address these details. Under these assumptions, the likelihood function is

$$l(\mathbf{m}) = \prod_{k=1}^K \frac{1}{(2\pi)^{N_k/2} |\mathbf{C}_k|^{1/2}} \exp\left(-\frac{1}{2} (\mathbf{d}_{obs,k} - \mathbf{d}_k(\mathbf{m}))^T \mathbf{C}_k^{-1} (\mathbf{d}_{obs,k} - \mathbf{d}_k(\mathbf{m}))\right), \quad (2)$$

where $|\cdot|$ denotes the matrix determinant, k indexes the various data types, and $\mathbf{d}_k(\mathbf{m})$ are predicted data with N_k being the number of data points. Estimating the covariance matrices \mathbf{C}_k is particularly important for Bayesian joint inference, where the contributions of various data sets to the solution are governed by these matrices. Therefore, each data type requires the estimation of a specific data covariance matrix. By considering eq. (2), the importance of the covariance matrix becomes clear since the

likelihood function depends on the number of observations in the various $\mathbf{d}_{obs,k}$. For instance, waveform data typically contain many more data points than amplitude spectra, since the sampling rate is typically high. Similarly, InSAR data contain pixels at a resolution far greater than the spatial wavelengths of features under investigation. The covariance matrices provide the appropriate statistical information that governs how much each data type contributes to the solution in eq. (1). Including full covariance matrices in joint inference provides the means to quantify uncertainty objectively, without the need for human-assigned weights.

Of particular interest is the covariance estimation for InSAR data. For the mainshock, the three available scenes exhibit different resolutions. To include these scenes in joint inference, the resolution must be accounted for by estimating a full covariance matrix for each scene including variance and covariance terms. We estimate non-Toeplitz covariance matrices⁶⁰ for the spatial InSAR scenes. The method is a combination of empirical iterative covariance estimates originally developed for frequency-domain reflection coefficient data⁶⁰ and nearest neighbor search⁶¹ via the k-nearest neighbor algorithm (KNN)^{62,63}, following methods developed for potential-field data⁶⁴. To estimate the covariance matrix, the SMC sampler initially assumes data noise to be uncorrelated with unknown standard deviation, similar to the approach implemented in BEAT for waveforms and amplitude spectra²¹. Subsequently, spatial data are binned via KNN clustering to estimate covariance terms. The approach also includes hierarchical scaling^{65,66} to lower the dependence of covariance matrix estimates on the iterative scheme.

A challenge arises from SAR scenes being acquired with substantial time between subsequent satellite passes (i.e., multiples of ~12 days, Supplementary Table S1, Fig. 7), resulting in multiple earthquakes contributing to the observed displacement fields. Acquisition times of SAR pairs are such, that the interferogram of track 020 includes only the first four inverted events, whereas both other tracks (122 and RCM) include six events (except those in March 2023, Supplementary Table S3). Consequently, it is likely, that the residual errors (Fig. 7) include contributions from fore- and aftershocks. This is also in agreement with track 020 having the highest VRs as it includes the least events. However, the difference in M_W between the mainshock and the next largest event is 0.5. In addition, the hypocenter depth of the mainshock is 1.25 km shallower than the next largest event. Therefore, such contributions are likely sufficiently small to be accounted for in the non-Toeplitz noise covariance estimate.

Earthquake source models. Source parameters are inferred by assuming point-source moment tensors⁶⁷ for the fore- and aftershocks of $M > 3.8$. Note that the moment tensors include unknown centroid locations and source-time function parameters, resulting in highly nonlinear inverse problems. In addition, moment tensors are considered in Lune space⁶⁸, which provides the advantage that parameter units are in degrees, making prior specifications simple compared to working with force-couples. The combination of high data quality and the availability of three InSAR scenes enables inferring parameters of spatial fault models for the mainshock. Bayesian inference for both a kinematic rectangular fault^{24,25} and a finite fault model^{28,69} are considered.

Uncertainty quantification and marginalization. All parameter inferences are based on the marginalization of the Bayesian posterior probability density, where the high-dimensional

posterior density is simplified by integrating over all parameters except those to be interpreted by the marginal probability. For example, the marginal density for centroid depth quantifies the probability of centroid depth while integrating over all other parameter values in the posterior. This process accounts for uncertainty due to the parameters that are integrated over (Supplementary Fig. S6a) and provides more general results than sensitivity studies. It is also useful to consider the marginal probability for two parameters (joint marginals) which illuminates the correlation of two parameters (Supplementary Fig. S6a). Finally, we employ the concept of marginalization to lower-hemisphere stereographic projections of the focal mechanism ("beach-balls"). We refer to these marginals of projections as fuzzy beach-balls (Supplementary Fig. S6b). Uncertainty estimates are taken to be the widths of 95% highest probability density credibility intervals estimated from marginal probabilities.

Stress inversion. Inferring the direction of principal stresses (stress inversion) is often hindered by insufficient knowledge of which nodal plane is the fault plane^{70,71}. We assigned the fault plane using an iterative process³³ by selecting the plane with the highest Mohr-Coulomb failure stress within a given stress field^{72,73}. We use 1000 random noise realizations in addition to the input nodal planes from the focal mechanisms for events with $M_W \geq 3.8$ (Fig. 1), over 100 bootstrap iterations for each inversion. This technique yields the orientation of the three principal compressive stresses ($\sigma_1 > \sigma_2 > \sigma_3$), as well as a relative measure of the magnitude of the intermediate principal stress (stress ratio, R)^{70,74}:

$$R = \frac{\sigma_1 - \sigma_2}{\sigma_1 - \sigma_3}, \quad (3)$$

with $0 \leq R \leq 1$. Small values of R suggest that σ_1 and σ_2 are close in magnitude, whereas large values of R suggest that σ_2 and σ_3 are similar in magnitude⁷⁵.

Earthquake relocation. An earthquake catalog²⁰ containing 132 events between November 23, 2022, and March 23, 2023, with the smallest event estimated to be M_L 1.93, is employed to study the spatial and temporal distribution of the seismicity. The catalog locations include many solutions with fixed depths. The accuracy of the few free depths is poor because the closest two stations are just over 70 km away and the third-closest station is at 130-km distance. Therefore, relocation based on picked catalog arrival times and up-sampled cross-correlations for earthquake pairs is applied. This method carries out an iterative, linearized inversion with re-weighting of data and automated discarding of poor data¹⁸. The final results are based on 150,000 data, of which 90.4% are retained to constrain the final result.

The relocation process reduces earthquake-pair differential time residuals of catalog phase arrivals from 0.42 s to 0.23 s and cross-correlations from 0.38 s to 0.05s. The reduction in cross-correlation residuals indicates that relative locations for events are improved by the relocation process. Reductions of cross-correlation residuals by a factor of 10 are common and emphasize the importance of including these data in the relocation procedure¹⁸. Absolute travel-time residuals remain similar (8.65 s and 8.63 s, Supplementary Fig. S10). Therefore, relative hypocentre locations are constrained well but absolute locations for the sequence are less well-constrained. For the interpretation presented here, relative locations are most important, and absolute locations are well-constrained for the largest event via the rectangular-fault solution that is constrained by InSAR and seismic data. Therefore, we apply a static shift for all relocations based on the difference between mainshock centroid moment

tensor and mainshock relocation. The shift is 1.5 km to the north, 1.8 km to the east, and 1 km deeper. Note that relocations that employ cross-correlation data are more sensitive to the centroid¹⁸. Since our results reduce cross-correlation based differential time residuals most, relocated event locations are likely closest to the centroid, not the focal point.

Uncertainties for relocated hypocenters are based on 1000 iterations of statistical resampling^{76,77}. This approach permits estimating standard errors for each hypocentre location. This approach permits estimating uncertainties for each location. The modes of the distributions of 95% credibility intervals are 93.1 m in longitude, 62.9 m in latitude, and 127.7 m in depth.

Data availability

Seismic data were accessed through IRIS Data Services (<https://ds.iris.edu>) which are funded by the National Science Foundation (EAR-1851048). The following seismic networks were used: AK⁷⁸, IE⁷⁹, C8⁸⁰, CN⁸¹, MB⁸², NY⁸³, PB⁸⁴, PQ⁸⁵, RV^{86,87}, TD⁸⁸, US⁸⁹, UW⁹⁰, XL⁹¹. The earthquake catalog is from Natural Resources Canada²⁰. The Sentinel-1 SAR data (Supplementary Table S1) is publicly available for download (<https://scihub.copernicus.eu/dhus/#/home>). Monthly injected volume data are available through Petrinex with IDs ABWI100141808217W500, ABWI100061408218W500 and ABWI100142508218W500. The post-processed InSAR data and the relocated earthquake catalog are available to download (<https://doi.org/10.6084/m9.figshare.24001752>). The formation data⁹³ are available from the Alberta Geological Survey (ags.aer.ca/research-initiatives/geological-framework).

Code availability

This work employed the open source libraries Bayesian Earthquake Analysis Tool (<https://pyrocko.org/beat>)¹⁹, Pyrocko (<https://pyrocko.org>)⁹⁴, Numpy⁹⁵, and Scipy⁶³. InSAR data were post-processed with KITE⁹⁶ (<https://pyrocko.org/kite>). Relocations are carried out with a Python implementation of hypo-DD¹⁸ which is available (<https://github.com/katie-biegel/relocDD-py>). Stress inversion was undertaken using STRESSINVERSE³³. The correlation analysis of seismicity and injection volumes was done by using ReshuffleCorr⁴¹ (<https://github.com/RyanJamesSchultz/ReshuffleCorr/>). Figures were produced with Matplotlib⁹⁷ and Generic Mapping Tools⁹⁸.

Received: 12 June 2023; Accepted: 19 October 2023;

Published online: 03 November 2023

References

- Schultz, R. et al. Disposal from in situ bitumen recovery induced the ML 5.6 Peace River earthquake. *Geophys. Res. Lett.* **50**, e2023GL102940 (2023).
- Alberta Energy Regulator (AER). *Announcement—November 30, 2022. Seismic Events Southeast of Peace River* <https://www.aer.ca/providing-information/news-and-resources/news-and-announcements/announcements/announcement-november-30-2022> (2022).
- Eaton, D. W. *Passive Seismic Monitoring of Induced Seismicity: Fundamental Principles and Application to Energy Technologies* (Cambridge University Press, 2018).
- Zhang, H., Eaton, D. W., Li, G., Liu, Y. & Harrington, R. M. Discriminating induced seismicity from natural earthquakes using moment tensors and source spectra. *J. Geophys. Res. Solid Earth* **121**, 972–993 (2016).
- Shapiro, S. A., Huenges, E. & Borm, G. Estimating the crust permeability from fluid-injection-induced seismic emission at the KTB site. *Geophys. J. Int.* **131**, F15–F18 (1997).
- Horner, R., Barclay, J. & Macrae, J. Earthquakes and hydrocarbon production in the Fort St. John area of northeastern BC. *Can. J. Explor. Geophys.* **30**, 39–50 (1994).
- Baranova, V., Mustaqem, A. & Bell, S. A model for induced seismicity caused by hydrocarbon production in the Western Canada Sedimentary Basin. *Can. J. Earth Sci.* **36**, 47–64 (1999).
- Schultz, R., Stern, V. & Gu, Y. J. An investigation of seismicity clustered near the Cordell Field, west central Alberta, and its relation to a nearby disposal well. *J. Geophys. Res. Solid Earth* **119**, 3410–3423 (2014).
- Li, T. et al. Earthquakes induced by wastewater disposal near Musreau Lake, Alberta, 2018–2020. *Seismol. Res. Lett.* **93**, 727–738 (2021).
- Schultz, R., Park, Y., Aguilar Suarez, A. L., Ellsworth, W. L. & Beroza, G. C. *En echelon* faults reactivated by wastewater disposal near Musreau lake, Alberta. *Geophys. J. Int.* **235**, 417–429 (2023).

11. Bao, X. & Eaton, D. W. Fault activation by hydraulic fracturing in western Canada. *Science* **354**, 1406–1409 (2016).
12. Atkinson, G. M. et al. Hydraulic fracturing and seismicity in the Western Canada Sedimentary Basin. *Seismol. Res. Lett.* **87**, 631–647 (2016).
13. Schultz, R., Wang, R., Gu, Y. J., Haug, K. & Atkinson, G. A seismological overview of the induced earthquakes in the Duvernay play near Fox Creek, Alberta. *J. Geophys. Res. Solid Earth* **122**, 492–505 (2017).
14. Mahani, A. B. et al. Fluid injection and seismic activity in the northern Montney Play, British Columbia, Canada, with special reference to the 17 August 2015 Mw 4.6 induced earthquake. *Bull. Seismol. Soc. Am.* **107**, 542–552 (2017).
15. Barclay, J., Utting, J., Krause, F. & Campbell, R. Growth faulting and syntectonic casting of the Dawson Creek Graben Complex: a North American craton-marginal trough; carboniferous-Permian Peace River Embayment, western Canada. *AAPG Bull.* **75**, 6 (1991).
16. Eaton, D. W., Ross, G. M. & Hope, J. The rise and fall of a cratonic arch: a regional seismic perspective on the Peace River Arch, Alberta. *Bull. Can. Pet. Geol.* **47**, 346–361 (1999).
17. Wozniakowska, P., Eaton, D., Deblonde, C., Mort, A. & Haeri Ardakani, O. Identification of regional structural corridors in the Montney play using trend-surface analysis combined with geophysical imaging. *GSC Open File Rep.* **8814**, 1308 (2021).
18. Waldhauser, F. & Ellsworth, W. L. A double-difference earthquake location algorithm: method and application to the northern Hayward fault, California. *Bull. Seismol. Soc. Am.* **90**, 1353–1368 (2000).
19. Vasyura-Bathke, H. et al. The Bayesian Earthquake Analysis Tool. *Seismol. Res. Lett.* **91**, 1003–1018 (2020).
20. Natural Resources Canada. *Canadian National Earthquake Database*. Canadian Hazards Information Service. <https://doi.org/10.17616/R3TD24> (1985).
21. Vasyura-Bathke, H., Dettmer, J., Dutta, R., Mai, P. M. & Jónsson, S. Accounting for theory errors with empirical Bayesian noise models in nonlinear centroid moment tensor estimation. *Geophys. J. Int.* **225**, 1412–1431 (2021).
22. Gardonio, B., Jolivet, R., Calais, E. & Leclère, H. The April 2017 mw6.5 Botswana earthquake: an intraplate event triggered by deep fluids. *Geophys. Res. Lett.* **45**, 8886–8896 (2018).
23. Kanamori, H. & Brodsky, E. E. The physics of earthquakes. *Rep. Prog. Phys.* **67**, 1429 (2004).
24. Haskell, N. A. Total energy and energy spectral density of elastic wave radiation from propagating faults. *Bull. Seismol. Soc. Am.* **54**, 1811–1841 (1964).
25. Heimann, S. *A Robust Method to Estimate Kinematic Earthquake Source Parameters*. PhD thesis. University of Hamburg (2011).
26. Wang, R. A simple orthonormalization method for stable and efficient computation of Green's functions. *Bull. Seismol. Soc. Am.* **89**, 733–741 (1999).
27. Simons, M. et al. The 2011 magnitude 9.0 Tohoku-oki earthquake: mosaicking the megathrust from seconds to centuries. *science* **332**, 1421–1425 (2011).
28. Minson, S., Simons, M. & Beck, J. Bayesian inversion for finite fault earthquake source models I—theory and algorithm. *Geophys. J. Int.* **194**, 1701–1726 (2013).
29. Atzori, S. & Antonioli, A. Optimal fault resolution in geodetic inversion of coseismic data. *Geophys. J. Int.* **185**, 529–538 (2011).
30. Ragon, T., Sladen, A. & Simons, M. Accounting for uncertain fault geometry in earthquake source inversions—I: theory and simplified application. *Geophys. J. Int.* **214**, 1174–1190 (2018).
31. Wesnousky, S. G. Predicting the endpoints of earthquake ruptures. *Nature* **444**, 358–360 (2006).
32. Barclay, J., Krause, F., Campbell, R. & Utting, J. Dynamic casting and growth faulting: Dawson Creek Graben Complex, carboniferous–Permian Peace River Embayment, western Canada. *Bull. Can. Pet. Geol.* **38**, 115–145 (1990).
33. Vavryčuk, V. Iterative joint inversion for stress and fault orientations from focal mechanisms. *Geophys. J. Int.* **199**, 69–77 (2014).
34. Dahm, T. et al. Recommendation for the discrimination of human-related and natural seismicity. *J. Seismol.* **17**, 197–202 (2013).
35. Dahm, T., Cesca, S., Hainzl, S., Braun, T. & Krüger, F. Discrimination between induced, triggered, and natural earthquakes close to hydrocarbon reservoirs: a probabilistic approach based on the modeling of depletion-induced stress changes and seismological source parameters. *J. Geophys. Res.* **120**, 2491–2509 (2015).
36. Davis, S. D. & Frohlich, C. Did (or will) fluid injection cause earthquakes?—criteria for a rational assessment. *Seismol. Res. Lett.* **64**, 207–224 (1993).
37. Verdon, J. P., Baptie, B. J. & Bommer, J. J. An improved framework for discriminating seismicity induced by industrial activities from natural earthquakes. *Seismol. Res. Lett.* **90**, 1592–1611 (2019).
38. Foulger, G. et al. Human-induced earthquakes: E-PIE—a generic tool for evaluating proposals of induced earthquakes. *J. Seismol.* **27**, 21–44 (2023).
39. Eaton, D. W. & Salvage, R. O. Discriminating natural and injection-induced earthquakes in the presence of uncertainty: a case study in Alberta, Canada. In *SSA Annual Meeting* (Seismological Society of America, 2023).
40. Skoumal, R. J., Brudzinski, M. R. & Currie, B. S. Proximity of Precambrian basement affects the likelihood of induced seismicity in the Appalachian, Illinois, and Williston basins, central and eastern United States. *Geosphere* **14**, 1365–1379 (2018).
41. Schultz, R. & Telesca, L. The cross-correlation and reshuffling tests in discerning induced seismicity. *Pure Appl. Geophys.* **175**, 3395–3401 (2018).
42. Beroza, G. C. & Ellsworth, W. L. Properties of the seismic nucleation phase. *Tectonophysics* **261**, 209–227 (1996).
43. Shapiro, S., Patzig, R., Rothert, E. & Rindschwentner, J. Triggering of seismicity by pore-pressure perturbations: permeability-related signatures of the phenomenon. *Thermo-Hydro-Mechanical Coupling in Fractured Rock*, 1051–1066 (Springer Basel, 2003).
44. Scholz, C. H. Earthquakes and friction laws. *Nature* **391**, 37–42 (1998).
45. Werner, C., Wegmüller, U., Strozzi, T. & Wiesmann, A. Gamma SAR and interferometric processing software. In *Proc. ERS-ENVISAT Symposium*, Vol. 1620, 1620 (Citeseer, 2000).
46. Abrams, M., Crippen, R. & Fujisada, H. ASTER Global Digital Elevation Model (GDEM) and ASTER Global Water Body Dataset (ASTWBD). *Remote Sens.* **12**, 1156 (2020).
47. Goldstein, R. M. & Werner, C. L. Radar interferogram filtering for geophysical applications. *Geophys. Res. Lett.* **25**, 4035–4038 (1998).
48. Costantini, M. A novel phase unwrapping method based on network programming. *IEEE Trans. Geosci. Remote Sens.* **36**, 813–821 (1998).
49. Chen, C. W. & Zebker, H. A. Phase unwrapping for large SAR interferograms: statistical segmentation and generalized network models. *IEEE Trans. Geosci. Remote Sens.* **40**, 1709–1719 (2002).
50. Wang, R., Lorenzo-Martín, F. & Roth, F. PSGRN/PSCMP—a new code for calculating co- and post-seismic deformation, geoid and gravity changes based on the viscoelastic-gravitational dislocation theory. *Comput. Geosci.* **32**, 527–541 (2006).
51. Heimann, S. et al. A Python framework for efficient use of pre-computed Green's functions in seismological and other physical forward and inverse source problems. *Solid Earth* **10**, 1921–1935 (2019).
52. Herrmann, R. B. Computer programs in seismology: an evolving tool for instruction and research. *Seismol. Res. Lett.* **84**, 1081–1088 (2013).
53. Herrmann, R. B., Benz, H. & Ammon, C. Monitoring the earthquake source process in North America. *Bull. Seismol. Soc. Am.* **101**, 2609–2625 (2011).
54. Del Moral, P., Doucet, A. & Jasra, A. Sequential Monte Carlo samplers. *J. R. Stat. Soc. B Stat. Methodol.* **68**, 411–436 (2006).
55. Jaynes, E. T. *Probability Theory: The Logic of Science* (Cambridge University Press, 2003).
56. MacKay, D. J. *Information Theory, Inference and Learning Algorithms* (Cambridge University Press, 2003).
57. Yagi, Y. & Fukahata, Y. Introduction of uncertainty of Green's function into waveform inversion for seismic source processes. *Geophys. J. Int.* **186**, 711–720 (2011).
58. Duputel, Z., Agram, P. S., Simons, M., Minson, S. E. & Beck, J. L. Accounting for prediction uncertainty when inferring subsurface fault slip. *Geophys. J. Int.* **197**, 464–482 (2014).
59. Hamidbeygi, M., Vasyura-Bathke, H., Dettmer, J., Eaton, D. W. & Dosso, S.E. Bayesian estimation of non-linear centroid moment tensors using multiple seismic data sets. *Geophysical Journal International* **235**, 2948–2961 (2023).
60. Dettmer, J., Dosso, S. E. & Holland, C. W. Uncertainty estimation in seismo-acoustic reflection travel time inversion. *J. Acoust. Soc. Am.* **122**, 161–176 (2007).
61. Knuth, D. E. *The Art of Computer Programming: Volume 3: Sorting and Searching* (Addison-Wesley Professional, 1998).
62. Cover, T. & Hart, P. Nearest neighbor pattern classification. *IEEE Trans. Inf. Theory* **13**, 21–27 (1967).
63. Virtanen, P. et al. SciPy 1.0: fundamental algorithms for scientific computing in Python. *Nat. Methods* **17**, 261–272 (2020).
64. Ghalenoei, E., Dettmer, J., Ali, M. Y. & Kim, J. W. Trans-dimensional gravity and magnetic joint inversion for 3-D earth models. *Geophys. J. Int.* **230**, 363–376 (2022).
65. Malinverno, A. & Briggs, V. A. Expanded uncertainty quantification in inverse problems: hierarchical Bayes and empirical Bayes. *Geophysics* **69**, 1005–1016 (2004).
66. Dettmer, J., Benavente, R., Cummins, P. R. & Sambridge, M. Trans-dimensional finite-fault inversion. *Geophys. J. Int.* **199**, 735–751 (2014).
67. Backus, G. & Mulcahy, M. Moment tensors and other phenomenological descriptions of seismic sources—I. continuous displacements. *Geophys. J. Int.* **46**, 341–361 (1976).
68. Tape, W. & Tape, C. A uniform parametrization of moment tensors. *Geophys. J. Int.* **202**, 2074–2081 (2015).

69. Olson, A. H. & Apsel, R. J. Finite faults and inverse theory with applications to the 1979 Imperial Valley earthquake. *Bull. Seismol. Soc. Am.* **72**, 1969–2001 (1982).
70. Gephart, J. W. & Forsyth, D. W. An improved method for determining the regional stress tensor using earthquake focal mechanism data: application to the San Fernando earthquake sequence. *J. Geophys. Res. Solid Earth* **89**, 9305–9320 (1984).
71. Michael, A. J. Use of focal mechanisms to determine stress: a control study. *J. Geophys. Res. Solid Earth* **92**, 357–368 (1987).
72. Lund, B. & Slunga, R. Stress tensor inversion using detailed microearthquake information and stability constraints: application to Ölfus in southwest Iceland. *J. Geophys. Res. Solid Earth* **104**, 14947–14964 (1999).
73. Vavryčuk, V. Principal earthquakes: theory and observations from the 2008 West Bohemia swarm. *Earth and Planet. Sci. Lett.* **305**, 290–296 (2011).
74. Etchecopar, A., Vasseur, G. & Daignieres, M. An inverse problem in microtectonics for the determination of stress tensors from fault striation analysis. *J. Struct. Geol.* **3**, 51–65 (1981).
75. Babaie-Mahani, A. et al. A systematic study of earthquake source mechanism and regional stress field in the Southern Montney unconventional play of northeast British Columbia, Canada. *Seismol. Res. Lett.* **91**, 195–206 (2020).
76. Efron, B. & Tibshirani, R. J. *An Introduction to the Bootstrap* (CRC Press, 1994).
77. Shearer, P. M. & Astiz, L. Locating nuclear explosions using waveform cross-correlation. In *Proc. 19th Ann. Seis. Res. Symp. Mon. CTBT*, 301–309 (1997).
78. Alaska Earthquake Center, Univ. of Alaska Fairbanks. *Alaska Geophysical Network* <https://www.fdsn.org/networks/detail/AK/> (1987).
79. Natural Resources Canada (NRCAN Canada). *GSC-BCOGC Induced Seismicity Study* https://www.fdsn.org/networks/detail/1E_2018/ (2018).
80. Natural Resources Canada (NRCAN Canada). *Canadian Seismic Research Network* <https://www.fdsn.org/networks/detail/C8/> (2002).
81. Natural Resources Canada (NRCAN Canada). *Canadian National Seismograph Network* <https://www.fdsn.org/networks/detail/CN/> (1975).
82. Montana Bureau of Mines and Geology/Montana Tech (MBMG, MT USA). *Montana Regional Seismic Network* <https://www.fdsn.org/networks/detail/MB/> (1982).
83. University of Ottawa (uOttawa Canada). *Yukon-Northwest Seismic Network* <https://www.fdsn.org/networks/detail/NY/> (2013).
84. UNAVCO. *Plate Boundary Observatory Borehole Seismic Network* <https://www.fdsn.org/networks/detail/PB/> (2004).
85. Geological Survey of Canada. *Public Safety Geoscience Program Canadian Research Network* <https://www.fdsn.org/networks/detail/PQ/> (2013).
86. Alberta Geological Survey/Alberta Energy Regulator. *Regional Alberta Observatory For Earthquake Studies Network* <https://www.fdsn.org/networks/detail/RV/> (2013).
87. Schultz, R. & Stern, V. The Regional Alberta Observatory for Earthquake Studies Network (RAVEN). *CSEG Recorder* **40**, 34–37 (2015).
88. TransAlta Corporation. *TransAlta Monitoring Network* <https://www.fdsn.org/networks/detail/TD/> (2013).
89. Albuquerque Seismological Laboratory (ASL)/USGS. *United States National Seismic Network* <https://www.fdsn.org/networks/detail/US/> (1990).
90. University of Washington. *Pacific Northwest Seismic Network* <https://www.fdsn.org/networks/detail/UW/> (University of Washington, 1963).
91. McGill University (Canada). *McGill Dawson-Septimus Induced Seismicity Study* https://www.fdsn.org/networks/detail/XL_2017/ (2017).
92. Vasyura-Bathke, H. et al. Earthquake catalog and InSAR data. figshare <https://doi.org/10.6084/m9.figshare.24001752> (2023).
93. Alberta Geological Survey. *3D Provincial Geological Framework Model of Alberta*, version 2 <https://ags.aer.ca/publication/3d-pgf-model-v2> (2019).
94. Heimann, S. et al. Pyrocko - An open-source seismology toolbox and library. *GFZ Data Services*. <https://doi.org/10.5880/GFZ.2.1.2017.001> (2017).
95. Harris, C. R. et al. Array programming with NumPy. *Nature* **585**, 357–362 (2020).
96. Isken, M. et al. *Kite—Software for Rapid Earthquake Source Optimisation from InSAR Surface Displacement*. V. 0.1 (GFZ Data Services, 2017).
97. Hunter, J. D. Matplotlib: a 2D graphics environment. *Comput. Sci. Eng.* **9**, 90–95 (2007).
98. Wessel, P., Smith, W. H. F., Scharroo, R., Luis, J. & Wobbe, F. Generic mapping tools: improved version released. *EOS Trans. AGU* **94**, 409–410 (2013).
99. Weides, S. N., Moeck, I. S., Schmitt, D. R. & Majorowicz, J. A. An integrative geothermal resource assessment study for the siliciclastic Granite Wash Unit, northwestern Alberta (Canada). *Environ. Earth Sci.* **72**, 4141–4154 (2014).
100. Alberta Geological Survey (AGS). *Alberta Table of Formations (Northwest Plains)* https://ags.aer.ca/publications/Table_of_Formations_2019.html (2015).

Acknowledgements

This work was funded by the DEEPEN project (GEO THERMICA; Bundesministerium für Wirtschaft und Energie, Germany, funding number 03EE4018), by Alliance Grant ALLRP 548576-2019, and by a Discovery Grant to J.D. from the Natural Sciences and Engineering Research Council of Canada (NSERC).

Author contributions

H.V.B., J.D. and D.W.E. designed the study and wrote the text. H.V.B. did seismic data processing and source inferences. K.B. carried out relocations; J.D. interpreted relocations; R.O.S. carried out stress inversions; D.W.E. compiled geologic information; S.S. provided and processed synthetic aperture radar data; N.A. generated and interpreted the initial earthquake catalog. J.D., H.V.B., D.W.E. and T.D. interpreted the results. H.V.B. produced the video animation. All authors contributed to editing the manuscript and producing figures.

Competing interests

The authors declare no competing interests.

Additional information

Supplementary information The online version contains supplementary material available at <https://doi.org/10.1038/s43247-023-01064-1>.

Correspondence and requests for materials should be addressed to Jan Dettmer.

Peer review information *Communications Earth & Environment* thanks Ryan Schultz and the other anonymous reviewer(s) for their contribution to the peer review of this work. Primary handling editors: Luca Dal Zilio and Joe Aslin. Peer reviewer reports are available.

Reprints and permission information is available at <http://www.nature.com/reprints>

Publisher's note Springer Nature remains neutral with regard to jurisdictional claims in published maps and institutional affiliations.



Open Access This article is licensed under a Creative Commons Attribution 4.0 International License, which permits use, sharing, adaptation, distribution and reproduction in any medium or format, as long as you give appropriate credit to the original author(s) and the source, provide a link to the Creative Commons licence, and indicate if changes were made. The images or other third party material in this article are included in the article's Creative Commons licence, unless indicated otherwise in a credit line to the material. If material is not included in the article's Creative Commons licence and your intended use is not permitted by statutory regulation or exceeds the permitted use, you will need to obtain permission directly from the copyright holder. To view a copy of this licence, visit <http://creativecommons.org/licenses/by/4.0/>.

© The Author(s) 2023